coatings

Article

Tribological Properties and Cutting Performance of AlTiN Coatings with Various Geometric Structures

Bin Li [1], Yuxiang Xu [1,*], Guoliang Rao [1], Qimin Wang [1,*], Jun Zheng [2], Ruiyuan Zhu [3] and Yubo Chen [3]

1   School of Electromechanical Engineering, Guangdong University of Technology, Guangzhou 510006, China
2   Key Laboratory of Green Fabrication and Surface Technology of Advanced Metal Materials,
    Ministry of Education, Anhui University of Technology, Ma'anshan 243000, China
3   Jiangxi Jiangwu Cemented Carbide Co., Ltd., Yichun 330699, China
*   Correspondence: yuxiang.xu@gdut.edu.cn (Y.X.); qmwang@gdut.edu.cn (Q.W.)

Abstract: The development of advanced machining techniques requires high-performance tool coatings. To improve the wear resistance and cutting performance of AlTiN coatings, a structure optimization strategy involving bias control and a nano-multilayer architecture strategy is presented. The investigated AlTiN coatings were deposited by cathodic arc evaporation and studied with regard to phase structure, hardness, adhesion, and tribological properties by a combination of X-ray diffraction, nanoindentation, scratch, and ball-on-disk friction tests. A high bias potential (up to -120 V) with enhanced adatom mobility suppressed the formation of the wurtzite structure AlN in AlTiN. In addition, the epitaxial growth of $Al_{0.67}Ti_{0.33}N$ on $Al_{0.5}Ti_{0.5}N$ in the AlTiN nano-multilayer could also promote the single-phase structure. The hardness of AlTiN-based coatings with a dominated cubic structure was 3–4 GPa higher than conventional ones. In addition, the interlayer interfaces in the $Al_{0.67}Ti_{0.33}N/Al_{0.5}Ti_{0.5}N$ multilayer could deflect the cracks and thus improve the fracture toughness. As a consequence, the $Al_{0.67}Ti_{0.33}N/Al_{0.5}Ti_{0.5}N$ multilayer with enhanced mechanical properties obtained the lowest wear rate of 1.1×10^{-5} $mm^3/N \cdot m$ and the longest cutting lifetime of 25 min during dry turning the SUS304 stainless steel.

Keywords: AlTiN; cathodic arc evaporation; structure design; mechanical properties; dry turning

1. Introduction

Transition metal nitrides are perfect for wear-resistant coatings on mechanical parts and cutting tools due to their high melting point and hardness. At the end of the 1980s, Al-containing AlTiN coatings were first explored [1]. The addition of Al significantly improved the mechanical properties and oxidation resistance [2]. The Al_2O_3 scale that forms on the AlTiN coating during machining slows heat transfer and thus better protects the tool material [3]. In addition, as demonstrated by Hörling et al. [4] and Mayrhofer et al. [5], the spinodal decomposition, originating from the supersaturated metastable state, leads to the age-hardening of AlTiN upon annealing. Excess Al content (typically greater than 65 at.% in the metal sublattice) results in the formation of wurtzite structured AlN in the as-deposited state, which reduces the mechanical properties of AlTiN coatings [6].

Nowadays, AlTiN is one of the most well-known hard coatings and has become a benchmark for metal cutting [7]. However, the development of advanced machining techniques (such as dry cutting) and the expanded applications of difficult-to-cut materials (such as Ti alloys) call for upgraded tool coatings. In recent years, improving the application ability of AlTiN coatings has attracted widespread attention in academia and industry. Different methods, such as alloying, multilayer architecture, and regulating deposition processes, have been employed to create high-performance AlTiN-based coatings. By adding alloy elements such as refractory Ta [8], self-lubricating V [9], and non-metallic Si [10], the thermal stability, oxidation resistance, and tribological properties can be well-tailored. The multilayer architecture can combine the benefits of various nitrides, and it is

feasible to improve hardness and toughness by rationally designing the modulation ratio and period [11–13]. The epitaxial growth associated with forming coherent or semi-coherent interfaces in nano-multilayer coatings can also tune the microstructure [14]. Dual-phase AlTiTaN and nanocomposite TiSiN can be stabilized as a cubic structure by nano-multilayer growth on AlTiN, obtaining excellent thermal stability [15,16]. In addition, the multilayer structure can also improve the corrosion resistance of AlTiN coatings by blocking the intrusion of corrosive media [17,18].

On the other hand, manipulation of the deposition process can also substantially affect the properties of tool coatings. Various physical vapor deposition techniques, involving cathode arc evaporation [19], magnetron sputtering [20], and hybrid arc-evaporation/sputtering [21], have been applied to deposit AlTiN coatings. Among them, cathodic arc evaporation has the merits of a high ionization rate and deposition efficiency and is widely used in the industrial production of tool coatings [22,23]. In addition to the Al content, deposition parameters play an essential role in the structure and properties of AlTiN coatings. A negative bias potential applied to the substrates can accelerate charged ions, leading to an ion bombardment effect and improved coating compactness [24,25]. Enhanced surface mobility of the deposited atoms can increase the solubility of Al in TiN, inhibiting the formation of wurtzite-structured AlN in AlTiN-based coatings [26,27]. Furthermore, nitride coatings with a high bias potential will have a high defect density and intrinsic stress [28,29]. High compressive residual stress is beneficial for increased hardness and wear resistance, while it can also reduce coating adhesion. A bilayer structure with a low bias at the bottom and a high bias at the top is a practical method for achieving good overall performance. A bottom layer with a low bias helps to improve the adhesion strength between the coating and the substrate. Additionally, a high bias at the top can enhance the mechanical properties, resulting in a better wear resistance. However, conventional AlTiN with a bilayer structure applying low and high bias exhibits moderate mechanical properties and is a universal tool coating grade. For high-speed dry cutting of stainless steel, it shows an apparent lack of performance [30]. Additionally, the relationship between structure, properties, and cutting performance is an essential scientific issue for tool coatings and needs further clarification. In this study, to improve the performance of conventional $Al_{0.67}Ti_{0.33}N$ coatings, two methods were adopted: gradient bias design up to −120 V and nano-multilayer architecture introducing $Al_{0.5}Ti_{0.5}N$. A comparative study was conducted on three AlTiN coatings concerning the structure and mechanical and tribological properties. Using continuous turning of SUS304 stainless steel, the cutting capabilities of coated inserts were evaluated explicitly in terms of tool wear.

2. Materials and Methods

2.1. Coating Deposition

AlTiN-based coatings with total thicknesses of ~3.0 μm were deposited on mirror-polished cemented carbide WC-6 wt.% Co blocks (with a hardness of 90 ± 2 HRA and dimensions of 16 × 16 × 4 mm) using an industry-scale arc evaporation system (INNOVA, Oerlikon Balzers, Balzers, Liechtenstein). Before being mounted on the substrate holder, the substrates were ultrasonically cleaned in deionized water, followed by anhydrous alcohol. When the chamber reached a base pressure of less than 5×10^{-3} Pa, an ion-etching procedure was carried out under an Ar pressure of 0.3 Pa and a bias voltage of −200 V for 30 min to remove contaminants from the substrate surface. Coating deposition was conducted at a temperature of 500 °C and a N_2 pressure of 3.5 Pa. In addition, the target current was set at 200 A. As illustrated in Figure 1, three coatings with different structures were deposited using specific parameters. The AlTiN_#1 coating was deposited from six $Al_{67}Ti_{33}$ targets (at.%, Ø160 × 12 mm in size) for 40 and 80 min, respectively, at bias potentials of 40 and 80 V. A gradient bias of −40 V to −120 V in steps of 20 V was applied to the AlTiN_#2 coating. For each bias potential, the dwell time was 24 min. For the AlTiN_#3 coating, an $Al_{0.67}Ti_{0.33}N$ interlayer with a thickness of 600 nm was first deposited at −40 V. Then, a nano-multilayer structure was achieved by substrate rotation between four $Al_{50}Ti_{50}$

and two $Al_{67}Ti_{33}$ targets with a bias potential of -80 V. According to a rotation speed of 2 rev/min and a deposition time of 96 min, a modulation period of ~12 nm was obtained for the AlTiN_3# coating.
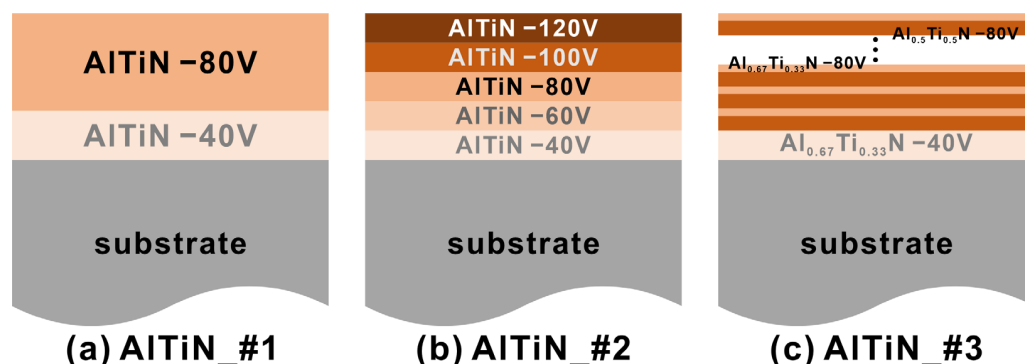
Figure 1. Schematic diagram of geometric structures for investigated coatings.

2.2. Coating Characterizations

The phase structures of the coatings were studied using grazing incidence X-ray diffraction (GIXRD, Bruker D8 Advance, Karlsruhe, Germany) operated at 40 kV and 40 mA with an incidence angle of $1°$. The hardness and elastic modulus of the coatings were measured using an instrumented nanoindenter (Anton Paar NHT^2, Corcelles, Switzerland) equipped with a Berkovich diamond tip, following the Oliver and Pharr method [31]. A maximum load of 10 mN was used to eliminate interference from substrates, achieving a penetration depth of less than 120 nm. Sixteen indents were measured for each sample to calculate the arithmetic mean and standard deviation. An Anton Paar Revetest scratch tester with a Rockwell C diamond tip (200 μm radius and $120°$ cone angle) was used to determine the adhesion strength between the coating and the substrate. The sliding distance was 3.0 mm, the normal load ranged from 1 to 100 N, and the loading rate was 100 N/min for scratch tests.

The coefficients of friction (CoF) of the coatings were recorded at room temperature (RT) using a ball-on-disk tribometer (Anton Paar THT1000, Corcelles, Switzerland) in an ambient atmosphere (relative humidity of ~45%). SUS304 stainless steel and alumina balls with a diameter of 6 mm were used as the counterpart materials. A normal force of 5 N, a track radius of 2.0 mm, and a sliding speed of 0.1 m/s were applied for friction tests. The wear resistance was evaluated via the specific wear rate, k, calculated according to the Archard equation: $k = V/(F \times L)$, where V is the wear loss (mm^3), F is the normal load (N), and L is the total sliding distance (m). The volume loss during wear was measured by a confocal laser scanning microscope (Olympus LEXT OLS4000, Tokyo, Japan) with a height resolution on the Z-axis of 10 nm.

Coated inserts (WC-6 wt.% Co, ISO CNMG120408-MA) for the machining of SUS304 stainless steel were tested using a CNC lathe (SMTCL ETC5075, Shenyang, China) at a cutting speed (v_c) of 150 m/min, a depth of cut (a_p) of 1.0 mm, and a feed rate (f) of 0.2 mm/rev. The wear of coated inserts was studied using a digital microscope (Keyence VHX, Osaka, Japan). The criterion for measuring tool life is when the maximum flank wear (VB_{max}) exceeds 0.2 mm.

3. Results and Discussion

3.1. Structural and Mechanical Properties

Figure 2 shows the GIXRD diffractograms of AlTiN_#1 to #3 coatings. For the AlTiN_#1 coating, three diffraction peaks in the 2θ range of 30–70° can be detected, corresponding to the (111), (200), and (220) crystalline planes of the face-centered cubic (FCC) structure, respectively. The XRD peaks of the AlTiN_#1 shift to a high 2θ angle compared to pure TiN (ICDD 00-038-1420, a = 4.24 Å), which can be attributed to the solid solution of Al into the

TiN lattice. Al atoms with a radius of 1.35 Å [32] are smaller than Ti atoms (1.40 Å) [32], and also, FCC AlN possesses a smaller lattice parameter (a = 4.12 Å, ICDD 00-025-1495). Therefore, the solid solution (Al, Ti)N exhibits a lattice parameter between TiN and AlN, which has been well documented in previous studies [33]. A weak diffraction signal at 2θ ~33.2° suggests the existence of wurtzite-structured AlN (ICDD 00-025-1133). With a gradient bias design from −40 to −120 V, the AlTiN_#2 coating shows a single FCC structure. The high bias provides more adatom mobility, contributing to the formation of a metastable FCC structure. It is worth noting that the detection depth of GIXRD is uncertain. Only the outermost coating information is reflected in the GIXRD diffractogram. A single FCC structure was also obtained for the AlTiN_#3 coating. According to a previous study [34], $Al_{0.67}Ti_{0.33}N$ can epitaxially grow on cubic $Al_{0.5}Ti_{0.5}N$, inhibiting wurtzite-structured AlN formation. Furthermore, the full width at half maximum (FWHM) of the (200) peak for AlTiN_#1, #2, and #3 coatings was 1.01°, 0.71°, and 0.79°, respectively. The larger FWHM of the AlTiN_#1 indicates a smaller grain size, which results from the competitive growth of cubic and wurtzite phases [35].
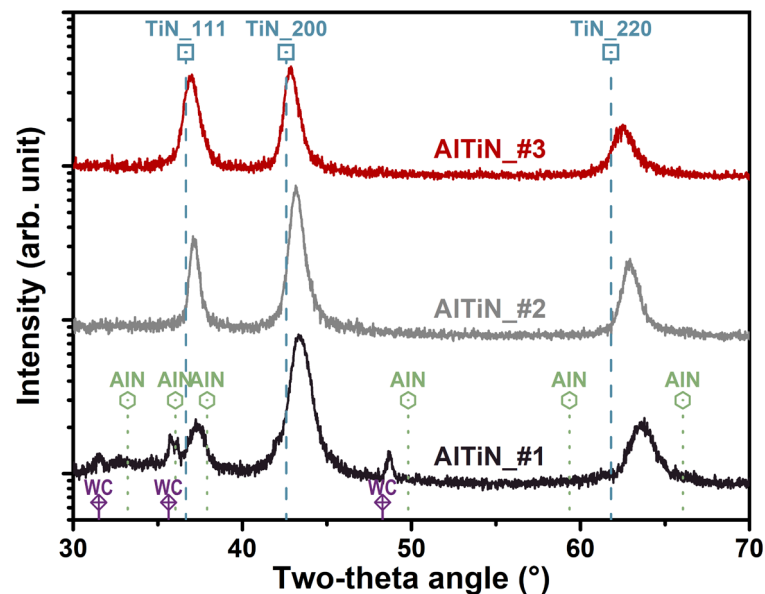

Figure 2. GIXRD diffractograms of AlTiN_#1, #2, and #3 coatings on cemented carbide substrates.

The nanoindentation hardness, H, and elastic modulus, E, are depicted in Figure 3, where the AlTiN_#1 coating shows an H and E of 28.2 ± 1.0 and 478 ± 9 GPa, respectively. When the bias potential was increased to −120 V, AlTiN_#2 has a dominating FCC structure and thus a higher H and E of 32.8 ± 0.8 and 528 ± 10 GPa, respectively. In addition, a high compressive residual stress, derived from a high substrate bias, could increase the hardness of AlTiN_#2 [36]. With a moderate bias of −80 V, the multilayer architecture by introducing $Al_{0.5}Ti_{0.5}N$ can also lead to a single-phase cubic structure, promoting increased mechanical properties. Additionally, the coherent strain at the interlayer interfaces could block dislocation movement and is conducive to hardness enhancement [37]. Therefore, when compared to AlTiN_#1, a higher H (31.6 ± 0.7 GPa) and E (536 ± 8 GPa) were obtained for the AlTiN_#3 coating.

Scratch tests with progressive loading were performed to examine the adhesion strengths of the three coatings. Figure 4 shows the optical images of scratch tracks left on AlTiN_#1, #2, and #3 coatings. All coating samples show typical scratch failure, including crack propagation and coating exfoliation. The crack initiation occurs inside the scratch tracks, which is related to the cohesive failure of AlTiN coatings. A further increase in normal load results in plenty of tensile-type cracks within the scratch tracks, as indicated in Figure 4. Moreover, longitudinal cracks at the edges of scratch tracks can be noticed. Here, the second critical load, L_{c2}, corresponding to the first adhesive spallation at the border

of the scratch track, is used to evaluate the adhesion strength of the coating on cemented carbide substrates. The AlTiN_#1 and #2 coatings show an L_{c2} of 74 and 77 N, respectively. When the load is larger than L_{c2}, a lot of adhesive spallation is detectable, and substrate exposure can be seen. In contrast, the AlTiN_#3 coating, with a slightly higher L_{c2} of 79 N, exhibits less flaking, suggesting an improved fracture toughness.
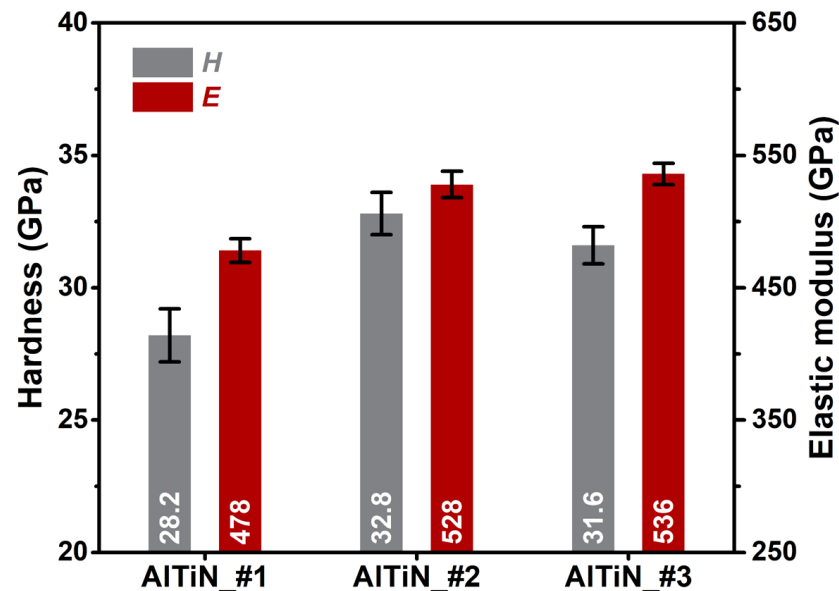

Figure 3. Nanoindentation hardness and elastic modulus of AlTiN_#1, #2, and #3 coatings.
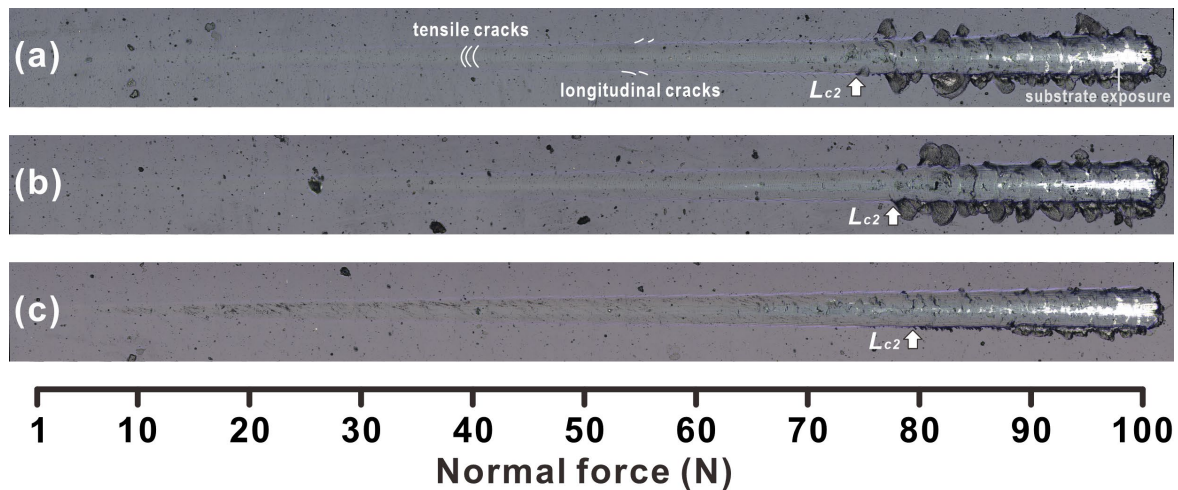

Figure 4. Optical scratch tracks left on (**a**) AlTiN_#1, (**b**) AlTiN_#2, and (**c**) AlTiN_#3 coatings.

3.2. Tribological Properties

Figure 5 shows the CoF curves of AlTiN coatings as recorded at RT. Two kinds of counterpart materials, SUS304 and polycrystalline Al_2O_3 balls, were used. All curves exhibit the characteristics of dry, non-intentionally lubricated sliding friction, where the CoF increases rapidly to the steady state. At the running-in stage, surface irregularities of the rubbing pair were quickly worn away, leading to more adhesion and a rise in friction [38]. The CoF enters a steady state as the friction surface is in complete contact. With stainless steel as the counterpart material, a significant fluctuation can be detected for all AlTiN coatings during the steady-state rubbing. The steady-state CoFs for AlTiN_1# (Figure 5a), AlTiN_#2 (Figure 5b), and AlTiN_#3 (Figure 5c) are 0.85 ± 0.10, 0.73 ± 0.14, and 0.82 ± 0.10, respectively. When the Al_2O_3 balls were applied, a comparable steady-state CoF

with a slight fluctuation could be obtained. The AlTiN_#1 coating (Figure 5d) reveals a CoF of 0.89 ± 0.02, and those of AlTiN_2# (Figure 5e) and AlTiN_3# (Figure 5f) are 0.85 ± 0.02 and 0.80 ± 0.03, respectively. As reported in the literature [39], AlTiN coatings exhibit a dry friction coefficient in the range of 0.5–0.85, which is affected by the counterpart materials.
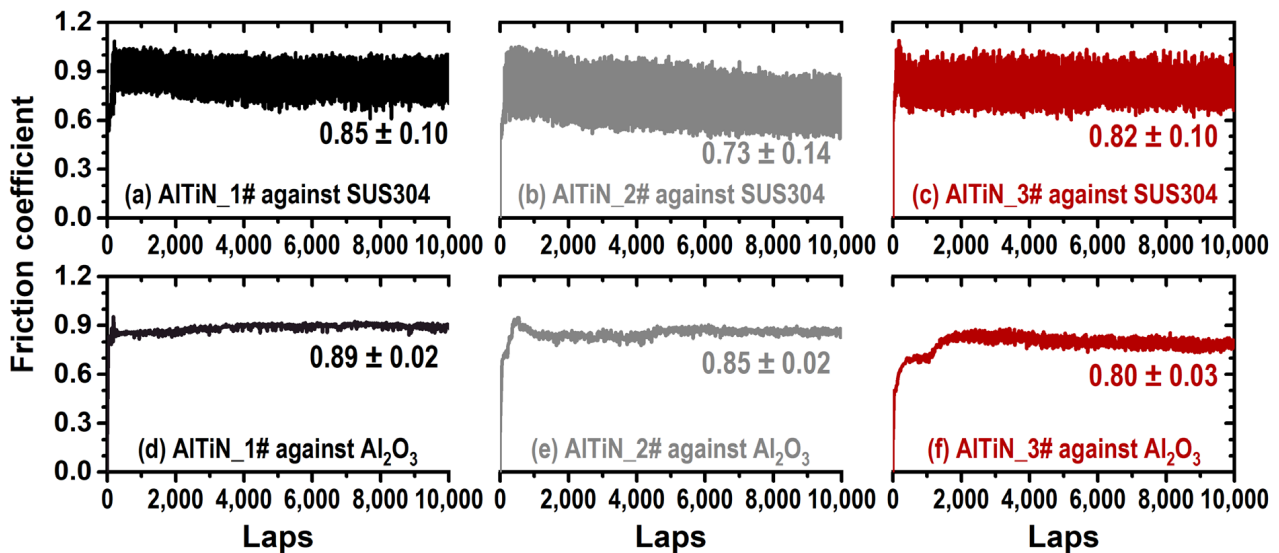
Figure 5. Friction curves of (**a**,**d**) AlTiN_#1, (**b**,**e**) AlTiN_#2, and (**c**,**f**) AlTiN_#3 coatings rubbed against (**a**–**c**) SUS304 and (**d**–**f**) Al$_2$O$_3$ balls.

After ball-on-disk tests, the wear tracks on AlTiN coatings were further investigated by confocal laser scanning microscopy, as displayed in Figure 6. Figure 6a–c shows the top views of wear tracks for AlTiN_#1, #2, and #3 coatings rubbed against SUS304. The SUS304 counterpart material almost covers the worn surface. Due to its lower hardness and high ductility, the SUS304 counterpart material tends to transfer to the hard coating surface, forming an oxygen-containing Fe-based transfer film [40]. The continuous formation and removal of transfer film cause a significant fluctuation in the friction curves, as seen in Figure 5a–c. For the specimens rubbed against Al$_2$O$_3$, the adherence of the counterpart materials on the wear tracks is hardly seen (Figure 6d–f). Some micro-furrows resulting from abrasive wear can be observed, especially on AlTiN_#1 and #2 coatings.

Additionally, the width of wear tracks when rubbed against Al$_2$O$_3$ is significantly smaller than in those rubbed against SUS304. Due to the high hardness of AlTiN coatings, only the SUS304 balls were severely worn, resulting in a large contact area. Additionally, the wear rate of the AlTiN coatings after sliding tests against SUS304 is negligible. Figure 7a–c shows the cross-sectional profiles of wear tracks left on AlTiN_#1, #2, and #3 coatings, respectively, after friction tests rubbed against Al$_2$O$_3$. The AlTiN_#1 and #2 coatings are almost worn through, which can be inferred from a considerable abrasion depth of ~3.0 μm. In contrast, the AlTiN_#3 coating has a shallow wear track, indicating mild wear. The calculated wear rates for the three coatings are depicted in Figure 7d. The AlTiN_#1 coating shows a wear rate of 2.2×10^{-5} mm^3/N·m. A slightly lower wear rate of 1.8×10^{-5} mm^3/N·m was obtained for the AlTiN_#2 coating. In agreement with the results of Liu et al. [41], the wear mechanism of AlTiN coatings at RT mainly consists of oxidation and abrasive wear. As a result of friction energy dissipation, a high flash temperature would induce the surface oxidation of coatings. Under repeated rubbing, the thin oxide scale was crushed to form oxide debris, including TiO$_2$ and Al$_2$O$_3$. Part of the oxide debris was discharged to the edge of the wear track, while another part of the oxide debris stayed in the wear track, acting as the medium for three-body abrasion. With higher hardness, AlTiN_#2 and #3 coatings have better resistance against abrasion than the AlTiN_#1. On the other hand, the AlTiN_#3 coating with the nano-multilayer

structure exhibits improved fracture toughness, which can reduce the production of wear debris. High hardness and well fracture toughness help increase the wear resistance of the AlTiN_#3 coating when rubbed against Al_2O_3. Therefore, the AlTiN_#3 coating shows the lowest wear rate of 1.1×10^{-5} $mm^3/N·m$, only half that of AlTiN_#1.
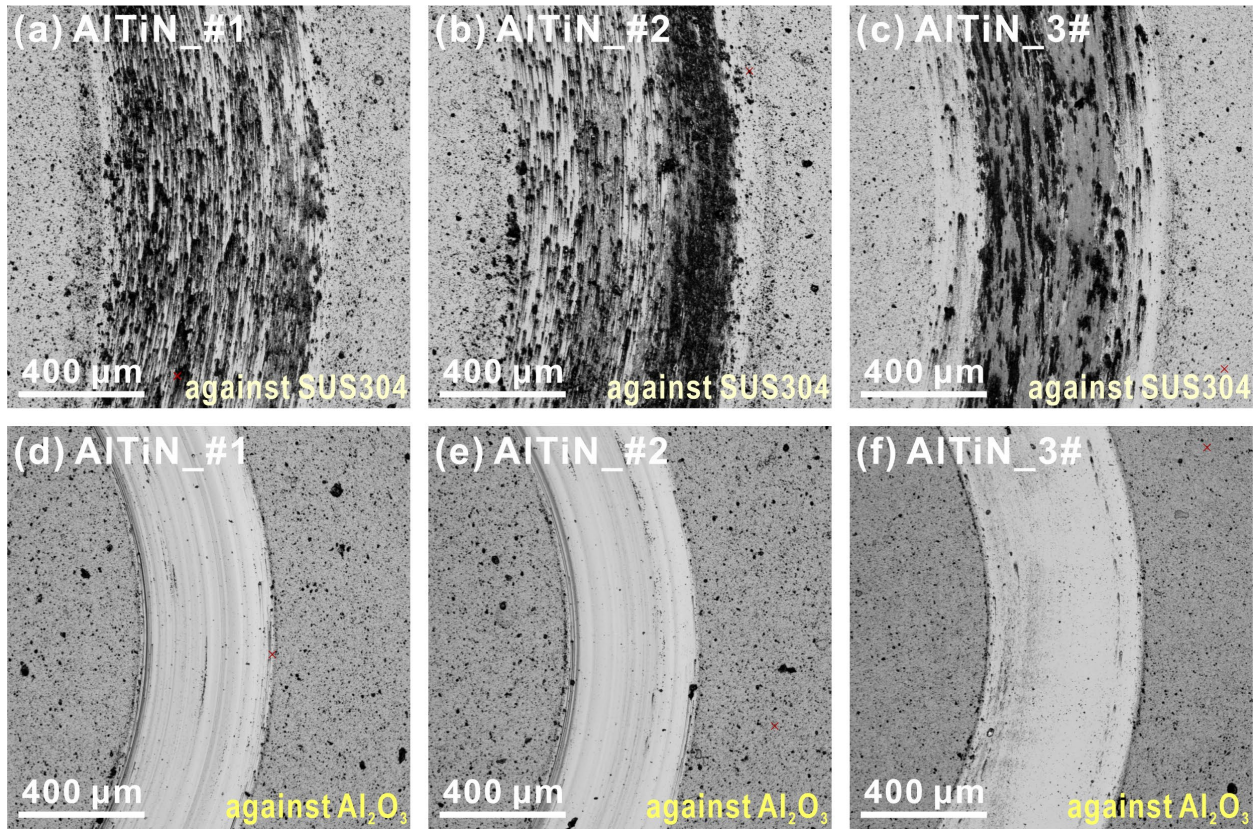

Figure 6. Top-views of wear tracks on (**a**,**d**) AlTiN_#1, (**b**,**e**) AlTiN_#2, and (**c**,**f**) AlTiN_#3 coatings after rubbing against (**a**–**c**) SUS304 and (**d**–**f**) Al_2O_3 balls.
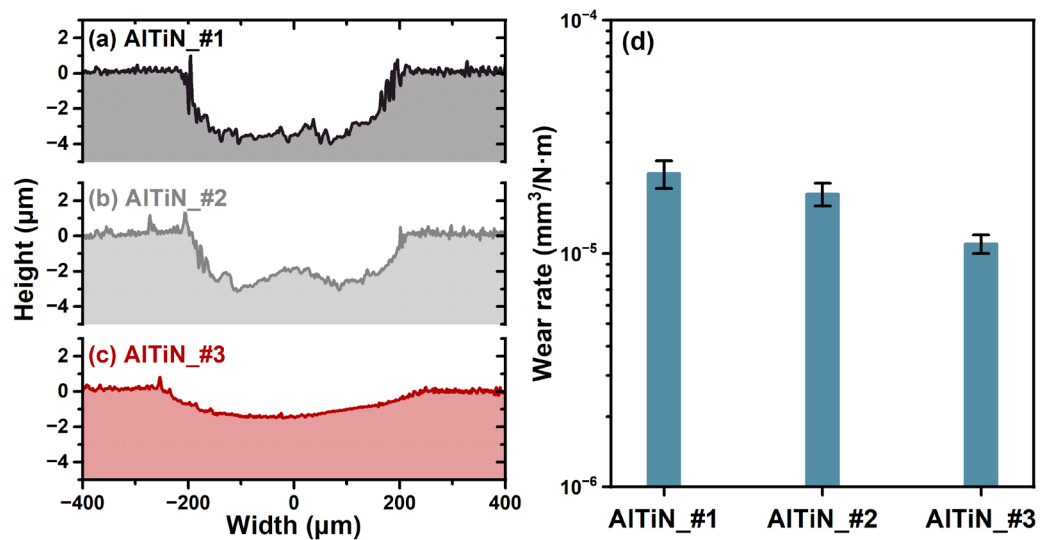

Figure 7. Cross-sectional profiles of wear tracks for (**a**) AlTiN_#1, (**b**) AlTiN_#2, and (**c**) AlTiN_#3 coatings after rubbing against Al_2O_3. (**d**) Calculated wear rates of various AlTiN coatings.

3.3. Cutting Performances

To further evaluate the machining performance of various coatings, drying turning tests on SUS304 stainless steel were carried out. Figure 8 presents the flank wear of coated inserts as a function of cutting time. With an increase in cutting time or cutting distance, the flank wear of the AlTiN_#1 coated insert continuously increases. The AlTiN_#1 coating fails at a cutting time of 21 min, in which the maximum depth of flank wear reaches 0.2 mm. The flank wear of the AlTiN_#2 and #3 coatings change in a similar way. The cutting lifetime of the AlTiN_#2 coating is about 20 min during the turning of SUS304 stainless steel. For the AlTiN_#3 coating, a longer cutting time before failure can be achieved. Owing to the improved hardness and fracture toughness with increased wear resistance, the AlTiN_#3 coating shows the best cutting performance with a turning lifetime of 25 min. In addition, the surface roughness of workpieces processed with different coated inserts is similar, with a value of 100 nm.
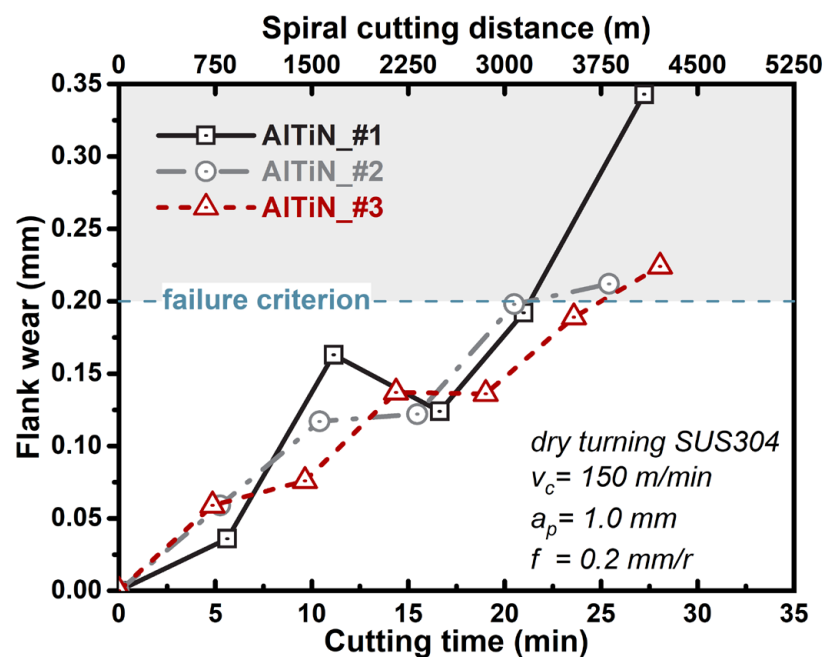

Figure 8. Flank wear of AlTiN_#1, #2, and #3 coated inserts during continuous turning of stainless steel.

Figure 9 shows the tool wear evolution of AlTiN_#1-, #2-, and #3-coated turning inserts. As seen from the optical images, the flank wear of tools increases with increasing cutting distance. Moreover, a built-up edge can be observed on the main cutting edge. The formation of a built-up edge is a well-known phenomenon at the tool–chip interface during the machining of ductile materials (such as stainless steel) [42]. The stability of cutting is affected by the built-up edge, which can be reduced by increasing the cutting speed. The notch wear can be seen from the top of the rake face, which occurs on both the rake and flank faces along the depth of cut. In short, the three AlTiN-coated inserts show similar tool wear during the dry turning of SUS304 stainless steel, including flank wear, notch wear, and built-up edge formation.
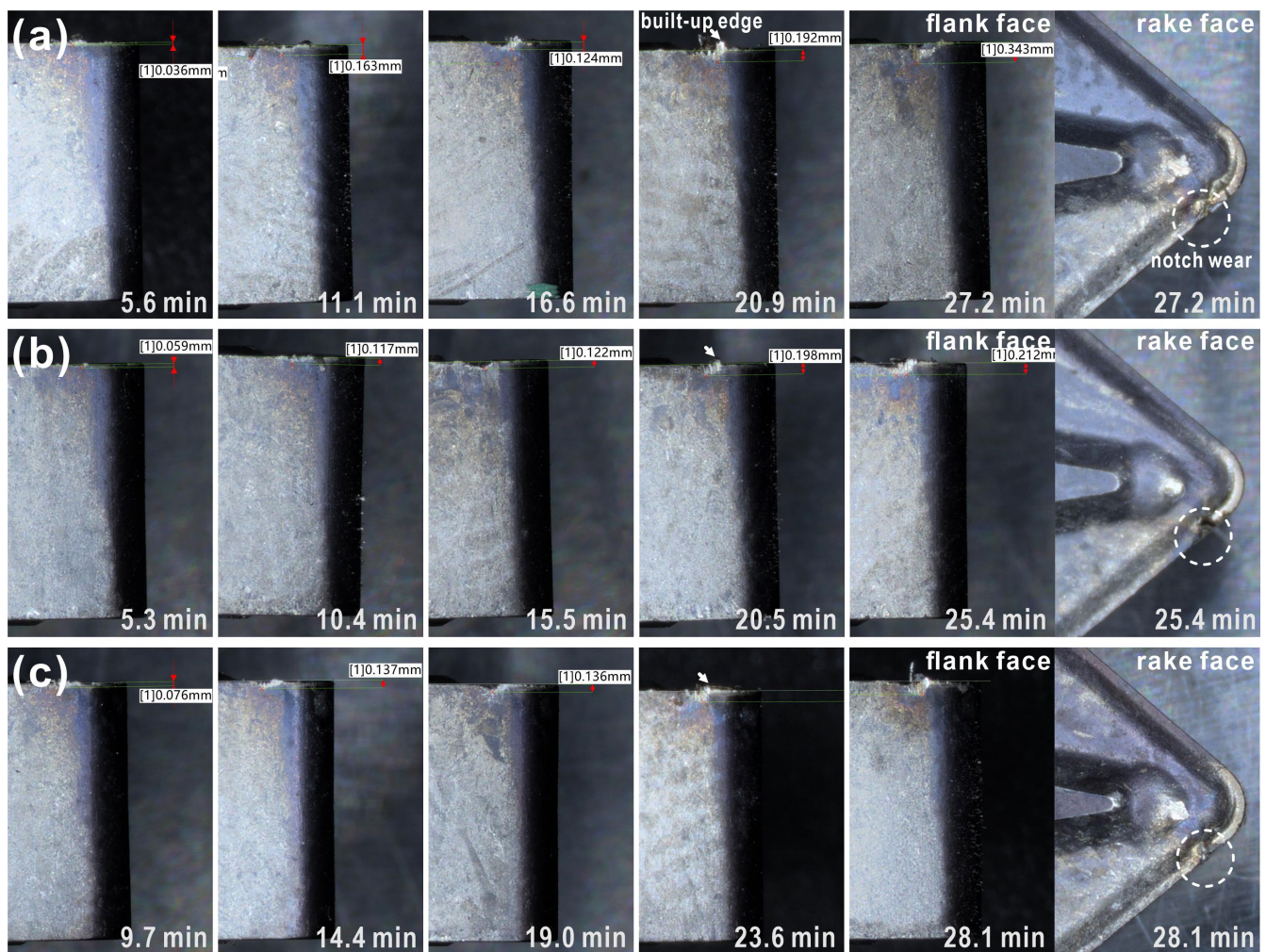
Figure 9. Tool wear as a function of cutting time of (**a**) AlTiN_#1-, (**b**) AlTiN_#2-, and (**c**) AlTiN_#3-coated inserts during turning of stainless steel.

4. Conclusions

The structural, mechanical, and tribological properties, as well as the cutting performance, of arc-evaporated AlTiN coatings with various geometric structures were investigated. According to the results, the study's principal findings can be summed up as follows:

(1) The conventional AlTiN_#1 coating shows a dual-phase structure consisting of cubic and wurtzite phases, exhibiting a hardness of 28.2 GPa. A high substrate bias in AlTiN_#2 and a nano-multilayer architecture in AlTiN_#3 result in a dominated cubic structure, increasing the hardness to greater than 31 GPa. In addition, the AlTiN_#3 coating has improved fracture toughness with good adhesion to cemented carbides.

(2) The wear process of AlTiN coatings was controlled by oxidation and abrasive wear. The synergistic enhancement in hardness and toughness significantly improved the wear resistance of the coating. The AlTiN_#3 coating shows a wear rate of 1.1×10^{-5} mm^3/N·m, which is lower than that of AlTiN_#1 and AlTiN_#2.

(3) The AlTiN_#3-coated insert manifests a superior cutting performance when turning SUS304 stainless steel, which might result from the enhanced mechanical properties and wear resistance. The lifetime of the AlTiN_#3 coating could increase by about 20% when compared to AlTiN_#1 and #2.

In summary, this work provides an effective and practical way to enhance the mechanical properties and wear resistance of AlTiN coatings via nano-multilayer architecture, which is promising for high-speed and dry-cutting applications.

References

1. Leyendecker, T.; Lemmer, O.; Esser, S.; Ebberink, J. The development of the PVD coating TiAlN as a commercial coating for cutting tools. *Surf. Coat. Technol.* **1991**, *48*, 175–178. [CrossRef]
2. Chen, L.; Paulitsch, J.; Du, Y.; Mayrhofer, P.H. Thermal stability and oxidation resistance of Ti–Al–N coatings. *Surf. Coat. Technol.* **2012**, *206*, 2954–2960. [CrossRef]
3. Münz, W.D. Titanium aluminum nitride films: A new alternative to TiN coatings. *J. Vac. Sci. Technol. A* **1986**, *4*, 2717–2725. [CrossRef]
4. Hörling, A.; Hultman, L.; Odén, M.; Sjölén, J.; Karlsson, L. Thermal stability of arc evaporated high aluminum-content $Ti_{1-x}Al_xN$ thin films. *J. Vac. Sci. Technol. A* **2002**, *20*, 1815–1823. [CrossRef]
5. Mayrhofer, P.H.; Hörling, A.; Karlsson, L.; Sjölén, J.; Larsson, T.; Mitterer, C.; Hultman, L. Self-organized nanostructures in the Ti–Al–N system. *Appl. Phys. Lett.* **2003**, *83*, 2049–2051. [CrossRef]
6. Waldl, H.; Tkadletz, M.; Lechner, A.; Czettl, C.; Pohler, M.; Schalk, N. Evolution of the fracture properties of arc evaporated $Ti_{1-x}Al_xN$ coatings with increasing Al content. *Surf. Coat. Technol.* **2022**, *444*, 128690. [CrossRef]
7. Schalk, N.; Tkadletz, M.; Mitterer, C. Hard coatings for cutting applications: Physical vs. chemical vapor deposition and future challenges for the coatings community. *Surf. Coat. Technol.* **2022**, *429*, 127949. [CrossRef]
8. Peng, B.; Li, H.; Zhang, Q.; Xu, Y.X.; Wei, T.; Wang, Q.; Zhang, F.; Kim, K.H. High-temperature thermal stability and oxidation resistance of Cr and Ta co-alloyed Ti–Al–N coatings deposited by cathodic arc evaporation. *Corros. Sci.* **2020**, *167*, 108490. [CrossRef]
9. Franz, R.; Mitterer, C. Vanadium containing self-adaptive low-friction hard coatings for high-temperature applications: A review. *Surf. Coat. Technol.* **2013**, *228*, 1–13. [CrossRef]
10. Liu, Z.R.; Pei, F.; Chen, L.; Mayrhofer, P.H. Effect of Si-addition on structure and thermal stability of Ti-Al-N coatings. *J. Alloys Compd.* **2022**, *917*, 165483. [CrossRef]
11. Xu, Y.X.; Chen, L.; Pei, F.; Chang, K.K.; Du, Y. Effect of the modulation ratio on the interface structure of TiAlN/TiN and TiAlN/ZrN multilayers: First-principles and experimental investigations. *Acta Mater.* **2017**, *130*, 281–288. [CrossRef]
12. Hahn, R.; Bartosik, M.; Soler, R.; Kirchlechner, C.; Dehm, G.; Mayrhofer, P.H. Superlattice effect for enhanced fracture toughness of hard coatings. *Scr. Mater.* **2016**, *124*, 67–70. [CrossRef]
13. Panjan, P.; Gselman, P.; Panjan, M.; Bončina, T.; Drnovšek, A.; Albu, M.; Čekada, M.; Zupanič, F. Microstructure and Surface Topography Study of Nanolayered TiAlN/CrN Hard Coating. *Coatings* **2022**, *12*, 1725. [CrossRef]
14. Li, Z.; Chen, L.; Zhang, J.; Sun, X. Structural, Mechanical, and Thermal Properties of the TiAlTaN/TiAlBN Multilayer. *Coatings* **2022**, *12*, 1951. [CrossRef]
15. Yang, Y.; Xu, Y.X.; Chen, L.; Mayrhofer, P.H. Improved Ti–Al–N coatings through Ta alloying and multilayer architecture. *Surf. Coat. Technol.* **2017**, *328*, 428–435. [CrossRef]
16. Peng, Y.H.; Chen, L.; Xu, Y.X.; Hu, C.; Du, Y. Interface enhanced mechanical and thermal properties of TiSiN/TiAlN multilayers. *J. Alloys Compd.* **2021**, *861*, 158571. [CrossRef]
17. Bilgin, S.; Güler, O.; Alver, Ü.; Erdemir, F.; Aslan, M.; Çanakçı, A. Effect of TiN, TiAlCN, AlCrN, and AlTiN ceramic coatings on corrosion behavior of tungsten carbide tool. *J. Aust. Ceram. Soc.* **2021**, *57*, 263–273. [CrossRef]
18. Mo, J.; Wu, Z.; Yao, Y.; Zhang, Q.; Wang, Q. Influence of Y-addition and multilayer modulation on microstructure, oxidation resistance and corrosion behavior of Al0.67Ti0.33N coatings. *Surf. Coat. Technol.* **2018**, *342*, 129–136. [CrossRef]
19. Andersson, J.M.; Vetter, J.; Müller, J.; Sjölén, J. Structural effects of energy input during growth of $Ti_{1-x}Al_xN$ ($0.55 \leq x \leq 0.66$) coatings by cathodic arc evaporation. *Surf. Coat. Technol.* **2014**, *240*, 211–220. [CrossRef]
20. Greczynski, G.; Lu, J.; Jensen, J.; Bolz, S.; Kölker, W.; Schiffers, C.; Lemmer, O.; Greene, J.E.; Hultman, L. A review of metal-ion-flux-controlled growth of metastable TiAlN by HIPIMS/DCMS co-sputtering. *Surf. Coat. Technol.* **2014**, *257*, 15–25. [CrossRef]
21. Zhang, Q.; Wu, Z.; Xu, Y.X.; Wang, Q.; Chen, L.; Kim, K.H. Improving the mechanical and anti-wear properties of AlTiN coatings by the hybrid arc and sputtering deposition. *Surf. Coat. Technol.* **2019**, *378*, 125022. [CrossRef]

22. Vetter, J. Vacuum arc coatings for tools: Potential and application. *Surf. Coat. Technol.* **1995**, *76–77*, 719–724. [CrossRef]
23. Anders, A. A review comparing cathodic arcs and high power impulse magnetron sputtering (HiPIMS). *Surf. Coat. Technol.* **2014**, *257*, 308–325. [CrossRef]
24. Mattox, D.M. Particle bombardment effects on thin-film deposition: A review. *J. Vac. Sci. Technol. A* **1989**, *7*, 1105–1114. [CrossRef]
25. Olbrich, W.; Fessmann, J.; Kampschulte, G.; Ebberink, J. Improved control of TiN coating properties using cathodic arc evaporation with a pulsed bias. *Surf. Coat. Technol.* **1991**, *49*, 258–262. [CrossRef]
26. Wüstefeld, C.; Rafaja, D.; Klemm, V.; Michotte, C.; Kathrein, M. Effect of the aluminium content and the bias voltage on the microstructure formation in $Ti_{1-x}Al_xN$ protective coatings grown by cathodic arc evaporation. *Surf. Coat. Technol.* **2010**, *205*, 1345–1349. [CrossRef]
27. Pfeiler, M.; Kutschej, K.; Penoy, M.; Michotte, C.; Mitterer, C.; Kathrein, M. The influence of bias voltage on structure and mechanical/tribological properties of arc evaporated Ti–Al–V–N coatings. *Surf. Coat. Technol.* **2007**, *202*, 1050–1054. [CrossRef]
28. Ahlgren, M.; Blomqvist, H. Influence of bias variation on residual stress and texture in TiAlN PVD coatings. *Surf. Coat. Technol.* **2005**, *200*, 157–160. [CrossRef]
29. Ljungcrantz, H.; Hultman, L.; Sundgren, J.E.; Karlsson, L. Ion induced stress generation in arc-evaporated TiN films. *J. Appl. Phys.* **1995**, *78*, 832–837. [CrossRef]
30. Hemmati, A.; DePaiva, J.M.; Veldhuis, S.C. An in-depth investigation of the machining performance of Ti1-Xalxn PVD coatings during high-speed machining of 316 stainless steel. *J. Manuf. Process.* **2022**, *75*, 903–918. [CrossRef]
31. Oliver, W.C.; Pharr, G.M. An improved technique for determining hardness and elastic modulus using load and displacement sensing indentation experiments. *J. Mater. Res.* **1992**, *7*, 1564–1583. [CrossRef]
32. Bragg, W.L. The arrangement of atoms in crystals. *Philos. Mag.* **1920**, *40*, 169–189. [CrossRef]
33. Ikeda, T.; Satoh, H. Phase formation and characterization of hard coatings in the Ti–Al–N system prepared by the cathodic arc ion plating method. *Thin Solid Films* **1991**, *195*, 99–110. [CrossRef]
34. Chen, L.; Xu, Y.X.; Du, Y.; Liu, Y. Effect of bilayer period on structure, mechanical and thermal properties of TiAlN/AlTiN multilayer coatings. *Thin Solid Films* **2015**, *592*, 207–214. [CrossRef]
35. Barna, P.B.; Adamik, M. Fundamental structure forming phenomena of polycrystalline films and the structure zone models. *Thin Solid Films* **1998**, *317*, 27–33. [CrossRef]
36. Skordaris, G.; Bouzakis, K.D.; Kotsanis, T.; Charalampous, P.; Bouzakis, E.; Breidenstein, B.; Bergmann, B.; Denkena, B. Effect of PVD film's residual stresses on their mechanical properties, brittleness, adhesion and cutting performance of coated tools. *CIRP J. Manuf. Sci. Technol.* **2017**, *18*, 145–151. [CrossRef]
37. Li, G.; Han, Z.; Tian, J.; Xu, J.; Gu, M. Alternating stress field and superhardness effect in TiN/NbN superlattice films. *J. Vac. Sci. Technol. A* **2002**, *20*, 674–677.
38. Blau, P.J. On the nature of running-in. *Tribol. Int.* **2005**, *38*, 1007–1012. [CrossRef]
39. Wang, X.; Kwon, P.Y.; Schrock, D.; Kim, D. Friction coefficient and sliding wear of AlTiN coating under various lubrication conditions. *Wear* **2013**, *304*, 67–76. [CrossRef]
40. Mo, J.L.; Zhu, M.H.; Leyland, A.; Matthews, A. Impact wear and abrasion resistance of CrN, AlCrN and AlTiN PVD coatings. *Surf. Coat. Technol.* **2013**, *215*, 170–177. [CrossRef]
41. Liu, A.; Deng, J.; Cui, H.; Chen, Y.; Zhao, J. Friction and wear properties of TiN, TiAlN, AlTiN and CrAlN PVD nitride coatings. *Int. J. Refract. Met. Hard. Mater.* **2012**, *31*, 82–88.
42. Ahmed, Y.S.; Fox-Rabinovich, G.; Paiva, J.M.; Wagg, T.; Veldhuis, S.C. Effect of built-up edge formation during stable state of wear in AISI 304 stainless steel on machining performance and surface integrity of the machined part. *Materials* **2017**, *10*, 1230. [CrossRef]